Stochastic hexagonal injectors in artificial spin ice

Robert Puttock, Anaïs Fondet, Ingrid Andersen, Mark Rosamond, Alexander Fernández Scarioni, Hans Schumacher, Etienne Snoeck, Christophe Gatel, Olga Kazakova

communications materials

Article

https://doi.org/10.1038/s43246-024-00614-0

Stochastic hexagonal injectors in artificial spin ice

Robert Puttock [1] ✉, Anaïs Fondet [2], Ingrid M. Andersen[2], Mark C. Rosamond[3], Alexander Fernández Scarioni [4], Hans W. Schumacher[4], Etienne Snoeck [2], Christophe Gatel [2,5] & Olga Kazakova [1] ✉

Artificial spin ice (ASI) systems have emerged as powerful platforms for exploring the fundamental aspects of magnetic frustration and topological phenomena in condensed matter physics. In this study, we investigate the bountiful effects that result from introducing hexagonal magnetic defects into an ASI lattice. The stochastic stabilisation of a plethora of metastable states in the hexagonal defects are explored, as well as harnessing the defect magnetisation state for the selective injection of emergent monopoles of different polarities and proximities within the lattice. We demonstrate a mechanism for tailoring the ASI behaviour using the magnetic state of the defect, which is of interest to applications including magnetic memory devices and spin-based logic.

Artificial spin ices (ASIs) represent a class of magnetic metamaterials that comprise of lithographically defined arrays of ferromagnetic nanoelements. The shape anisotropy of the nanoelements mean that they only possess two possible binary states, much like an Ising spin. While ASI were originally designed to model geometric frustration in more complicated three-dimensional structures, they now form a subset of research within their own right as they are tailorable through the geometrically arranged pattern design and material composition[1–3].

Localised topologically-protected excitations, sometimes called emergent magnetic monopoles, can be nucleated and propagated under external stimuli including electromagnetic fields, and temperature[4–8]. The topological states, and collective dynamic behaviour, exhibited by ASI have applications as both reconfigurable spin-waveguides and as hardware realisations of low-energy computing[9–11]. The ability to tailor and manipulate the physical properties of the system with the array design allows for specific control of the magnetic ordering in both the ground and excited states at the will of the designer[12–16].

For example, chiral lattice geometries have been shown to exhibit a thermal ratchet behaviour in the ASI lattice[17]. Whereas the inclusion of geometric[18,19] and topological[20] defects has a profound effect on the local magnetisation of the lattice structure in response to perturbative stimuli. In addition, the inclusion of parallel nanoislands in the lattice design promotes ferro-/antiferromagnetic coupling and the formation of non-Ising vortex states within the nanoelements[21–23].

Vortices are one of the fundamental spin configurations occurring in magnetic nano-disks, arising from the geometric confinement of the spins to reduce the counteracting energy components of both magnetostatic and exchange energy. Their structure is characterised by both the chirality of the rotation of spins clockwise/counterclockwise (CW/CCW, respectively) and the polarity of the out-of-plane spin at the centre of the vortex. These two degrees of freedom and their inherent stability have made them promising candidates for non-volatile and high-density data storage in, e.g., spin nano oscillators[24,25]. Vortices in ASI have also gained interest in their application to alternative computing, where their spontaneous formation and dynamics are of interest for reservoir computing paradigms[11,26–28].

The magnetic state of the nano-disks heavily relies on their geometric parameters and thermal stability, as well as the field history, where S- or C-shaped magnetic textures may prevail over collinear or vortex states[29,30]. When nano-disks are integrated into 2D arrays, both the inter-object magnetic coupling, and intra-magnetic state of each nano-disk, influences the collective magnetic order and thermal dynamics, exhibiting order-disorder phase transitions under the shifting spin dimensionality within the nano-disks[31,32].

Here, the result of the intra- and inter-magnetic coupling within the defect ASI arrays are explored. The influence and behaviour of vortices and other metastable domain configurations within hexagonal defect ASIs (HDASI) are demonstrated to be controlled injectors of magnetostatic excitations into the surrounding ASI lattice. Nanoscale hexagonal defects promote a more complex energy landscape compared to circular nano-disks due to their inherent shape anisotropy and edge-based domain-wall pinning locations. As such, the stable formation of exotic magnetic textures is promoted. We show that the lattice-defect coupling leads to the formation of a plethora of stochastically formed metastable states within the defect that are not typically stabilised. The magnetic coupling between these configurations

[1]National Physical Laboratory, Hampton Road, Teddington, UK. [2]Centre d'Elaboration de Materiaux et d'Etudes Structurales, CNRS, Toulouse, France. [3]School of Electronic and Electrical Engineering, University of Leeds, Leeds, UK. [4]Physikalisch-Technische Bundesanstalt, Bundesallee 100, Braunschweig, Germany. [5]Université Paul Sabatier, Université de Toulouse, Toulouse, France. ✉e-mail: robb.puttock@protonmail.com; olga.kazakova@npl.co.uk

and the lattice result in interesting variations of switching behaviours within the ASI lattice at the defect proximity. In addition, the chirality of a vortex within the defect is shown to enable selective injection of positive and negative excited states into the ASI lattice. This has great implications for controlling the dynamics in ASI as vortex states can be controlled by numerous regimes, which enables a direct read-write mechanism in a hybrid ASI lattice.

Results

Part A - Metastable remanent magnetic configurations

The HDASI lattice is comprised of a kagome permalloy design ($t = 20$ nm) with hexagonal defects situated within the negative space of select unit cells (see Methods). Figure 1 shows the magnetic configuration of the stable vortex in the hexagonal defect within a kagome lattice. The over-focused Lorentz transmission electron microscopy (LTEM) micrograph of the HDASI lattice at zero-field, Fig. 1a, shows magnetic contrast. For example, the black point at the centre of the hexagonal structure indicates the presence of a magnetic vortex with a CW orientation.

From LTEM images obtained at different focal lengths, the magnetic induction in the defect and surrounding nanowires was acquired using the transport of intensity equation (TIE). The resulting M_x and M_y components, shown in Fig. 1c(i-ii), confirm the CW chirality of the vortex[33–35]. The micromagnetic structure in Fig. 1b was modelled by utilising the object-oriented micromagnetic framework (OOMMF) simulation software[36]. The M_x and M_y components of the simulation in Fig. 1d(i-ii), concur with the experimental data.

Vortices are the expected magnetic configuration of a hexagonal structure of this size, but the defect coupling to the ASI lattice also promotes the stabilisation of alternative magnetic domain configurations. Figure 2a(i) displays the LTEM micrographs of the hexagonal defect in its vortex state, alongside its other frequent metastable magnetic configurations: Y-shaped, striped, and eye-domain (Fig. 2b(i)-d(i), respectively). These states were realised by saturating the HDASI lattice along the x-axis (to the right of the image) under the same field conditions and then subsequently relaxing the field to zero (see Methods). These states were distributed across several defect sites in the same lattice, as seen in Supplementary Fig. S1 in the supplementary information (SI).

Figure 2a-d(ii) replicate the remanent domain configurations achieved through micromagnetic modelling. During the initial investigation, the full multitude of states did not readily form in the model upon repeated field operations. This indicates that the stochastic formation of several states, as seen in the experiments, is the result of uncaptured intrinsic or extrinsic factors, such as lithographic effects. Instead, the micromagnetic states were replicated in silico by applying spatially varying applied field protocols to break the system symmetry (see methods).

The calculated total and demagnetisation energy components for the four states at remanence are plotted in Fig. 2e (red circles and blue squares, respectively). The graph shows that the total energy (E_{tot}) of the system is dominated by the demagnetisation energy component (E_{ms}) and that the three metastable states in Fig. 2b–d are incredibly similar in energy profile ($E_{tot} = 0.435$, 0.429, and 0.437 fJ, respectively). By comparison, the vortex state has a lower total energy of 0.313 fJ, confirming that it is the preferred ground state. The energy gap between E_{tot} and E_{ms} is primarily the exchange energy component (E_{ex}), which is an order of magnitude smaller than E_{ms} and near constant across all four domain configurations. The energetic similarities between metastable states depicted in Fig. 2 provide a reasonable explanation for their readiness to stochastically form in the experimental system. The coupling of the hexagonal defect to the ASI lattice, and the defect's shape anisotropy, promotes domain wall pinning and makes metastable domain configuration more than a hexagon of these dimensions in isolation.

In Supplementary Section S2 of the SI, micromagnetic modelling was used to study the angular dependence magnetic state formation for the lattice; initialised with a vortex domain state as depicted in Fig. 2a(ii). The results show that the Y-shaped magnetic domain configurations readily formed when the field was applied exactly along the x-axis (i.e., parallel to one of the nanowires). Whereas the striped and eye-shaped magnetic domain configurations readily formed with a misalignment applied field. By contrast, the vortex did not readily stabilise by the in-plane saturation method.

To understand the stochastic domain formation better, the micromagnetic state of the hexagonal defects is evaluated within the ASI network as a function of the field. To achieve this, a different HDASI system was designed with a single column of alternating hexagonal defects set into the ASI network that allows for simultaneous imaging of multiple states (Fig. 3). The states were recorded using magnetic force microscopy (MFM), which spatially maps the stray field above the sample surface using a magnetic coated probe[37]. Here, an electromagnet is fitted into the microscope configuration to allow for imaging with the applied field in situ (see Methods).

Figure 3a(i-ii) presents the topography, and corresponding magnetic stray-field contrast, of the alternating HDASI network at remanence, respectively. The initial magnetic state, depicted in Fig. 3a(ii), was achieved by applying a quasi-static field pulse $\mu_0 H = -60$ mT (to the right of the page).

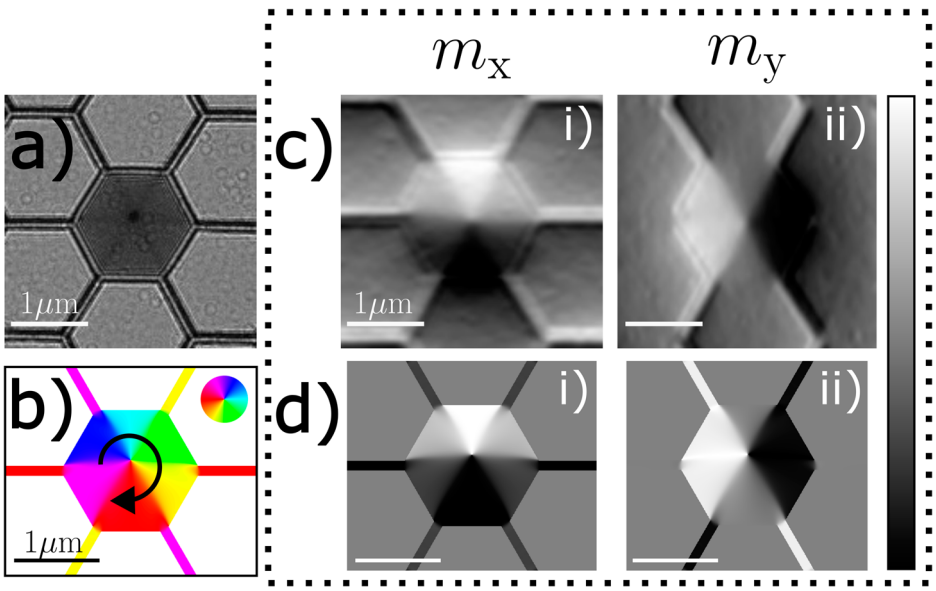

Fig. 1 | Hexagonal defect ASI with vortex. a Over-focused Lorentz transmission electron micrograph (LTEM) depicting the magnetic configuration of the Kagome artificial spin ice (ASI) lattice with a solid hexagonal defect. **b** Modelled magnetisation configuration (colour represents angle of the magnetic vector with respect to the x-axis) of the clockwise vortex configuration of the hexagonal defect set into the ASI lattice. **c** Reconstituted phase map that depicts the x and y components of the magnetisation vector (i and ii, respectively) confirming the clockwise chirality of the vortex determined by solving the transport-of-intensity equation. **d** Simulated maps of the magnetisation vector x and y components (i and ii, respectively).

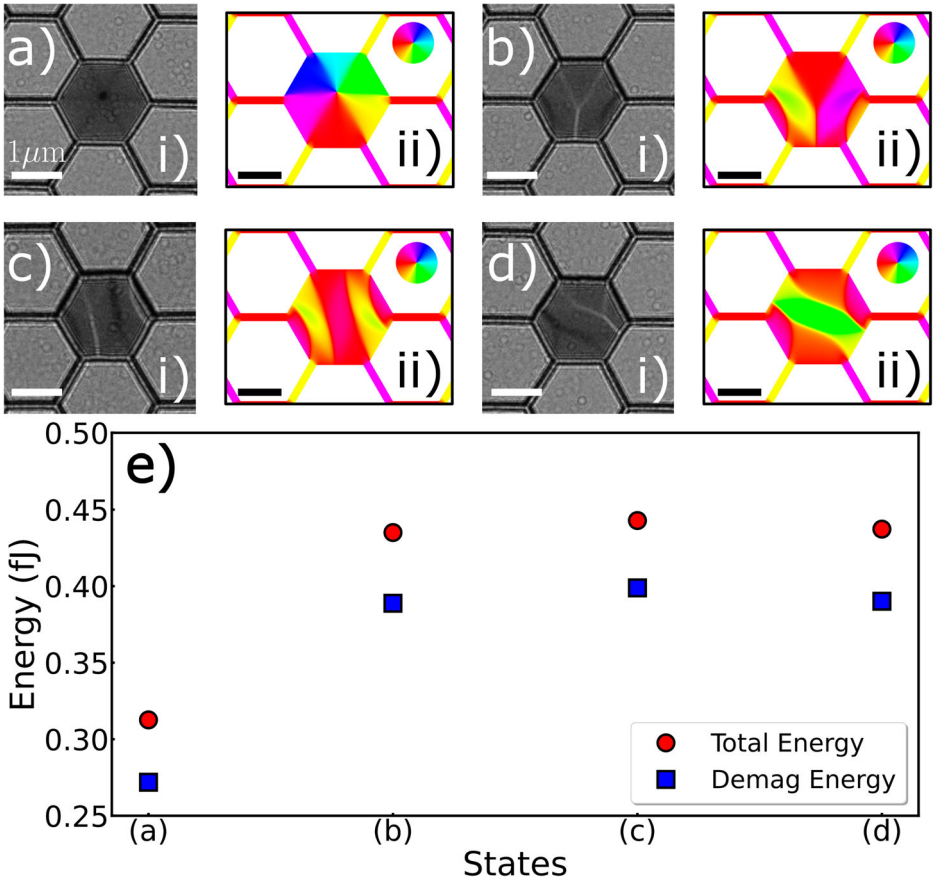

Fig. 2 | Metastable magnetisation structures in HDASI. a–d Cropped LTEM micrographs (i) and matching modelled magnetisation maps (ii) of the vortex-, Y-, striped-, and eye-domain magnetic domain configurations of the hexagonal defect at remanence set into the ASI lattice (**a**–**d**, respectively). Scale bars are 1 μm. **e** Modelled total and demagnetisation energies (red circles and blue squares, respectively) of the four ASI magnetic states depicted in **a**–**d**.

The resulting magnetic state of the ASI lattice follows the applied field direction, and the magnetisation of the hexagonal defects all form a striped domain pattern like that shown in Fig. 2c.

Figure 3a(iii) depicts the magnetic state of the alternating hexagonal lattice under an applied field of $\mu_0 H = 10$ mT directed to the left of the page. Here, the defects lose their uniformity and an assortment of domain states form stochastically, which can be differentiated by their MFM contrast. Vortices of both CW and CCW chiralities formed in six of the defects within the image window. The chirality is determined by the offset position of the core normal to the field direction and relative to the hexagon centre. This is depicted in more detail in Fig. 3b(i-iv), where the initial striped domain configuration collapses into a CCW vortex at $\mu_0 H = 10$ mT. Increasing the field further results in the core being pushed to the defect edge until the defect is fully saturated at $\mu_0 H = 30$ mT.

The contrast of the vortices is distinct from the eye-domain, which forms in four of the defects in the image window (marked E in Fig. 3a(iii)). Here, a domain that is aligned with the field direction forms in the centre of the defect, with domain walls pushed to the hexagonal defect's edges.

Upon releasing the field, the magnetic states relax to vortex and eye domain configurations (Fig. 3a(iv)) at remanence. The states are conserved at remanence relative to when the field is applied in Fig. 3a(iii), including the individual vortex chiralities. In some cases, the vortex does not fully form a coherent rotation within the hexagonal defect at remanence, which results in strong edge contrast (e.g., top of Fig. 3a(iv)). This is due to domain wall pinning at the defect-lattice interface and is explored in greater detail in Supplementary Section S3 in the SI and in the following section.

To better understand the magnetic phase diagram of the system, statistical analyses were performed on the domain configurations of the hexagonal defects under different field magnitudes. The lattice was saturated each time ($\mu_0 H = -60$ mT), then the field is released to form the magnetic configuration depicted in Fig. 3a(i). Subsequently, the magnetic field was applied and released, and the states were recorded and analysed at zero-field after 10 mT. 20 mT and 30 mT quasi-static field pulses.

The sample size was set to $n = 4$ images per field, and this process was repeated for all fields. The resulting mean population frequency of states, $\bar{p}$, is shown in Fig. 3c. The sequence in Fig. 3a was not included in the statistical analysis as the process of raster-scanning the MFM probe during field application as capturing Fig. 3a(iii) resulted in a different field history for the lattice compared to the other data sets. The combination of the MFM probe's stray field and the in situ field did impact the magnetic configurations of the hexagonal defect, as evidenced by the reduction in the number of striped domain states in Fig. 3a(iii) compared to the statistical analysis at the same field.

Part B - emergent monopole injection

The distribution of states after a field was applied between 20 and 30 mT coincides with the start of monopole injection from the defect into the lattice at neighbouring vertex junctions. This opens the question as to whether the defect's magnetic state has an impact on monopole injection and dynamics. This section explores monopole injection effects as a function of the field and the initial magnetic configuration of the defect. In kagome ASI, the emergent monopole is positioned where the vertex junction charge (Q), composed of 3 nanowire charges (q), exceeds the charge value of the background vertices in the lattice (Q_0). Thus, emergent magnetic monopoles charges are defined as vertices with $\Delta Q = Q - Q_0 = \pm 2q$ providing their population is dilute[3].

First, the angular dependence of the HDASI lattice is evaluated through micromagnetic modelling (see Methods). The initial state of the modelled ASI lattice before each measurement has a net magnetisation component pointing towards the left of the page, at remanence, and a CW vortex state is stabilised in the defect (as depicted in Fig. 4b(i)). The vertices have an initial chequerboard configuration of +q and -q states as is typical for a kagome ground state. The lattice is subjected to a field $\mu_0 H = 25$ mT at an angle, θ,

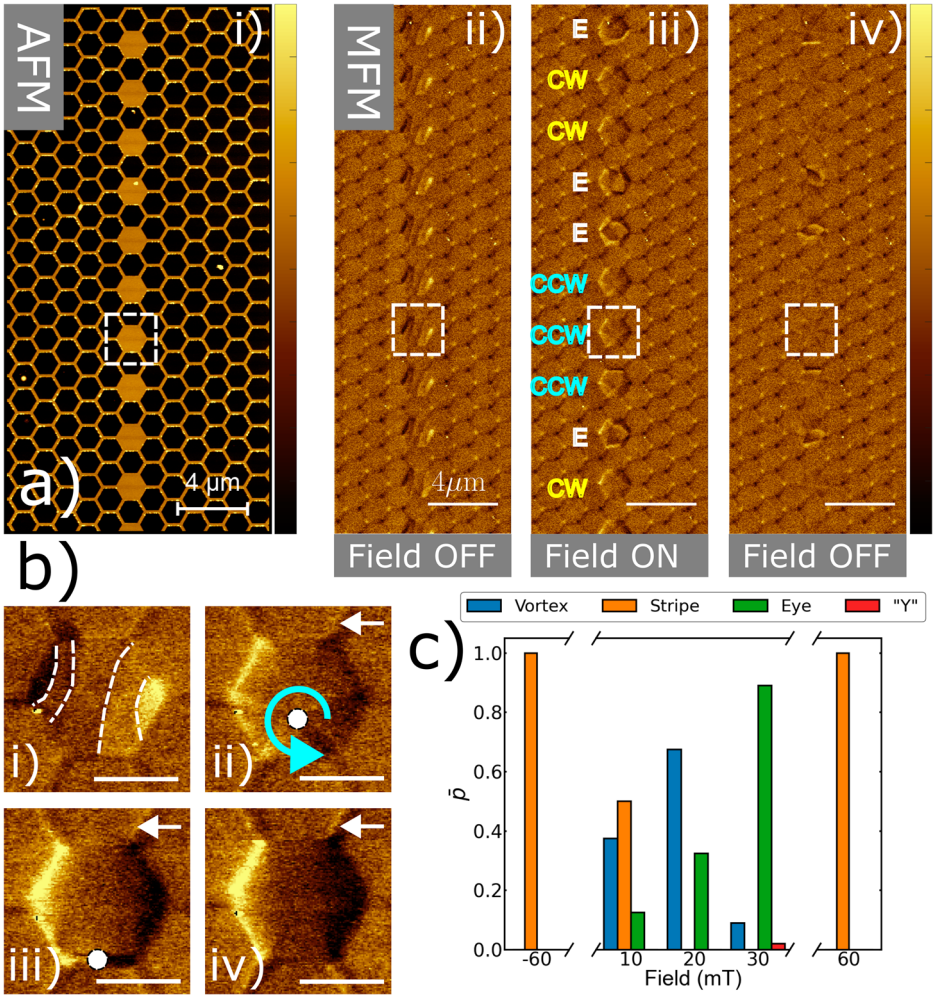

Fig. 3 | Magnetic force microscopy statistics. a (i) Atomic force micrograph (AFM) of the alternating hexagonal defect ASI lattice. (ii-iv) Magnetic force microscopy (MFM) images of the lattice at: (ii) zero field after saturation along the image *x*-axis in applied field $\mu_0 H = -60$ mT; (iii) $\mu_0 H = 10$ mT; and (iv) $\mu_0 H = 0$ mT, respectively. Eye-, and clockwise/counterclockwise vortex-domain configurations are marked on (ii) as E, CW, and CCW, respectively. **b** MFM image of a hexagonal defect undergoing field reversal at $\mu_0 H = 0 - 30$ mT in 10 mT increments (i-iv, respectively), scale bars represent 1 μm. The core of the vortex moving downwards with respect to increasing applied field along the *x*-axis is indicative of a CCW chirality. **c** Mean population frequency ($\bar{p}$) of the four common states formed at zero field, as depicted in Fig. 2, after different field histories. Statistics were gathered from MFM images of 10 hexagonal defects in each image, with a minimum image sample number of N = 4 per field, where the sample was reset each time by a saturating field $\mu_0 H = -60$ mT.

relative to the *x*-axis applied in the opposite direction of the initialised state. Figure 4a depicts the net planar magnetisation components (m_x and m_y) of the HDASI lattice magnetisation as a function of the applied field angle.

The gradual linear background of the magnetisation components throughout the measurement sequence is a result of the canting of spins in the HDASI lattice in the applied field. This is particularly biased by the spins within the defect itself as they have a weaker shape anisotropy compared to the ASI nanowires. Sharp changes to the magnetisation components throughout the modelling sequence are indicative of nanowire switches in the ASI lattice surrounding the defect. This is expected as the defect-lattice coupling creates injection sites as a function of field angle as described in previous works[19]. There is a symmetrical monopole injection into the nanowire either side of the defect at field angles below $\theta = 39°$. Additional switches in magnetisation are observed above and below the defect for nanowires aligned with the applied field direction.

At angles between 39 and 54°, the simulations show that there is a monopole injection symmetry breaking as nanowires aligned along the *x*-axis only switch on one side of the defect. Figure 4b(i-iii) displays the magnetic configuration of HDASI with CW vortex for $\theta = 46°$ and field magnitudes $\mu_0 H = 0$ mT, 20 mT, and 25 mT, respectively. Figure 4b(iii) depicts a monopole injection in the nanowire to the right of the defect and an absence of nanowire switching to the left. Within the defect area shown in Fig. 4b(ii), it is possible to see the displacement of the vortex core under the applied field $\mu_0 H = 20$ mT, as well as the presence of domain wall pinning sites where the nanowires meet the hexagonal defect corners (i.e., the defect-nanowire interface). It is this magnetic confinement that results in the injection asymmetry under a slightly greater field in Fig. 4b(iii).

For comparison, the same simulations were performed on just a hexagonal defect (i.e., in the absence of the surrounding ASI structure) in Supplementary Section S4 of the SI. Under applied field, the magnitude of the m_x and m_y components of the defect are at parity when $\theta = 46°$. The alignment of the magnetisation vector within the defect around this angle appears to assist propagation and promote monopole injection asymmetry.

Figure 4c presents simulation snapshots of the HDASI system under the same field protocol except a CCW vortex is present at the centre of the hexagonal defect at remanence. Here, the core displacement is inverted under the applied field, compared to Fig. 4b, which results in a reversal of the monopole injection asymmetry. In addition, the sign of the monopole injected into the lattice is also inverted due to its proximity to the defect.

The defect system is also evaluated under the same field protocol when initialised with the eye-domain state in Fig. 4d. Here, we see that the eye-domain state undergoes a different magnetic domain transition than the vortex states under the same applied field, resulting in a symmetric monopole injection. The simulations show that the symmetry is preserved in this field angle window resulting in monopole injection on both sides of the defect.

Figure 4e plots the curl of magnetisation ($\nabla \times M$) for vortex and eye-domain states along profiles depicted in Fig. 4b(ii) and 4d(ii) (blue and red profiles, respectively). The curl of the magnetisation indicates the local variations of magnetic field strength originating from the variations in spins canting. Positive (negative) signs of $\nabla \times M$ denote CCW (CW) field rotation. For the CW vortex, sharp peaks with positive signs occur at the defect-nanowire interface, inducing nanowire switching under greater applied field due to the right nanowire experiencing a high magnetic flux density. The left

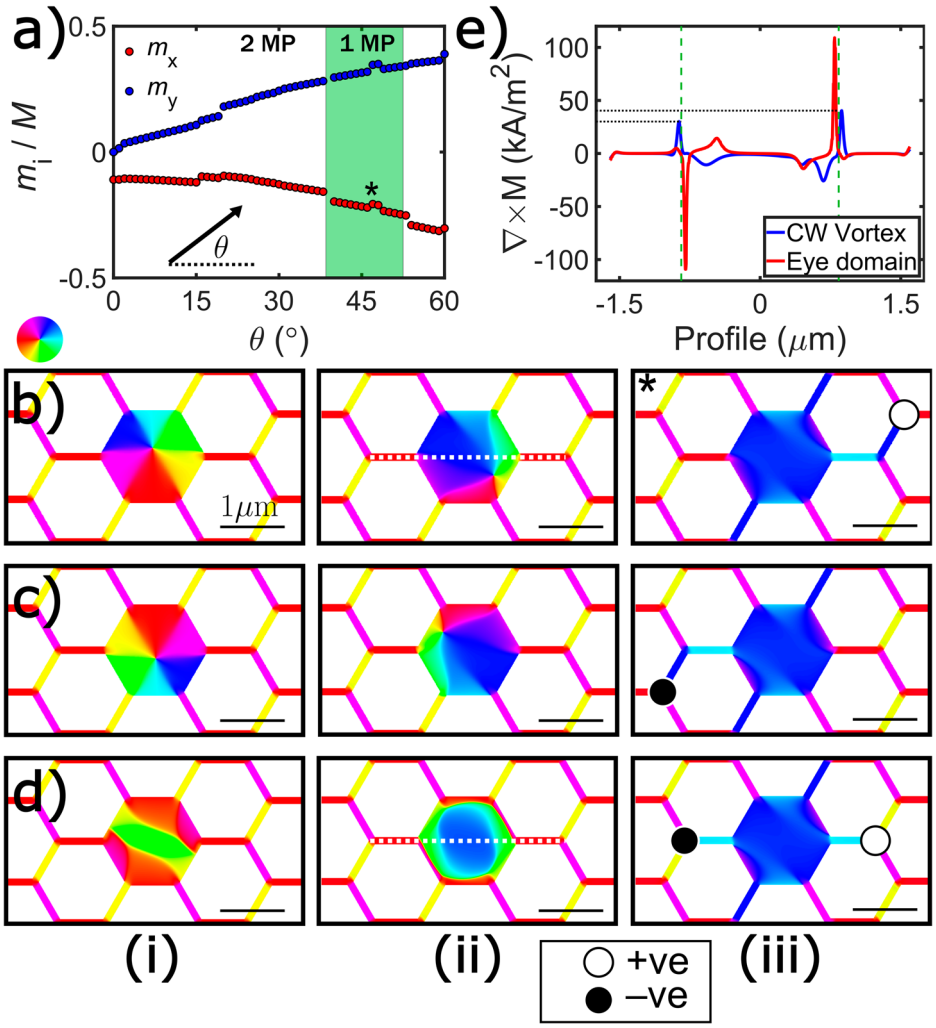

Fig. 4 | Micromagnetic modelling. a Plot of the modelled net magnetisation components, m_x and m_y, as a function of applied field angle, θ, and field magnitude $\mu_0 H = 25$ mT, for the HDASI lattice when the defect is initialised with a CW vortex domain. Shaded green region depicts the field angles between which only one monopole (MP) is injected into the ASI lattice. **b-d** Simulated magnetisation maps of the HDASI lattice undergoing field reversal at θ = 46°, $\mu_0 H = 0$ mT, 20 mT and 25 mT (i-iii, respectively), when the defect is initialised with a CW and CCW vortices, and eye domain configuration, respectively. **e** Line profiles of the curl of the magnetisation (∇×M) for vortex and eye-domain states along profiles depicted in b(ii) and d(ii) (white dashed lines, and dashed green lines indicate the edge of the defect).

side shows lower peak-trough magnitudes, indicating weaker flux density and explains the asymmetric nanowire switching (Fig. 4b(iii)) when the applied field is increased.

In contrast, the eye-domain's ∇×M profile is highly antisymmetric, showing large and sharp peaks/troughs from the coherent spin rotation of the domain wall in the defect. The interaction at the defect-nanowire interface is an order of magnitude weaker compared to the vortex state, resulting in symmetric switching in both nanowires as the domain wall is pushed further towards the defect edges under increased field at the next field step (Fig. 4d(iii)).

Figure 5 aims to replicate the main findings from Fig. 4 under experimental conditions using LTEM (see Methods). Due to the nature of the experimental setup, a large out of plane (OOP) field is present throughout the measurement sequence, see Methods, which was not present in the micromagnetic modelling. A test in OOMMF was performed with and without an OOP field that showed the OOP field component did greatly reduce the magnitude of the in-plane field required to saturate the defect. The OOP field had a greater effect on the defect magnetisation compared to the ASI nanowires because of the differences in shape anisotropy. The impact of this is explored further in Supplementary Section S5 in the SI and in the Discussion.

In Fig. 5, the lattice is saturated at an angle of approximately 45° from the horizontal parallel bars (see Methods). This is different from the modelling in Fig. 4 where the saturation angle was along the x-axis. This initialisation direction still results in a chequerboard ground state of +q and -q charge states on the vertices, but the charge state is inverted from the initialised state presented in Fig. 4b-d(i). Simulations confirmed that this change in starting state for the ASI did not impact the asymmetric switching mechanism (Supplementary Fig. S6 in the SI).

After saturation, the HDASI lattice is imaged at zero-field, revealing the initial magnetic configuration of the lattice. The field is subsequently applied in the opposite direction and the micromagnetic configuration is recorded at ~1 mT intervals. This enables tracking of the defect's internal magnetic structure, as well as the switches of the nanowires surrounding the defect site. Arrows in Fig. 5 indicated the magnetisation direction of the nanowires surrounding the defect. Supplementary Figs. S7-9 in the SI demonstrates a full range of LTEM images throughout the switching sequence.

Figure 5a depicts the initial magnetised state of the HDASI lattice with a CCW vortex in the centre of the defect and ASI magnetisation directed to the bottom-left of the page. An in-plane applied field magnitude ($\mu_0 H_{\parallel}$) of 15 mT was applied to the lattice at θ = 45° in Fig. 5b (yellow arrow). The LTEM contrast of some nanowires have inverted perpendicular to their length, which indicates a magnetisation reversal. As such, the diagonal nanowires aligned with the field, above and below the defect, have switched as well as the nanowire to the left of the defect. This asymmetric nanowire switching behaviour along the *x*-axis has closely matched the micromagnetic simulations displayed in Fig. 4c(iii).

Figure 5c shows the same initialised state as Fig. 5a in the ASI lattice, but the vortex within the defect has stabilised with a CW chirality. In Fig. 5d, when this magnetic configuration was exposed to the same field conditions as in Fig. 5b, the asymmetric switching along the x-axis was not present, thus

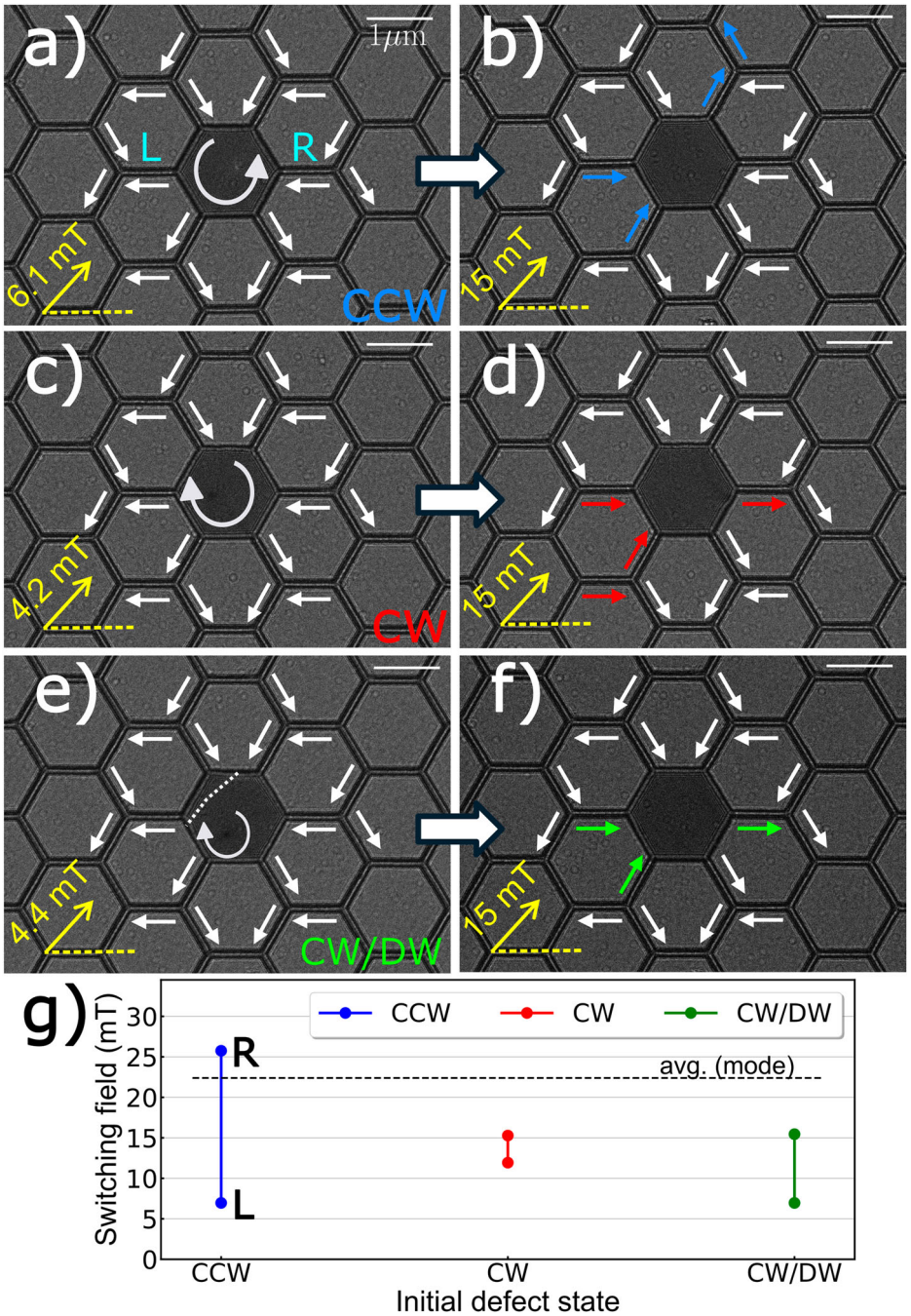

Fig. 5 | Selective injection. a, b Over-focused LTEM micrographs for the HDASI lattice when **a** initialised with a CCW vortex in the defect centre and **b** after application of an in-plane applied field $\mu_0 H_{||} = 15$ mT and $\theta = 45°$. **c**–**f** Equivalent LTEM micrographs depicting the magnetic states for the same HDASI lattice measurement sequence, except the defect was initialised with a CW vortex **c**, **d** and CW vortex with domain wall (CW/DW) **e**, **f**, respectively**. g** Plot of the $\mu_0 H_{||}$ magnitudes required to switch the nanowires to the left (L) and right (R) of the defect for the three initialised conditions in a-e: CCW, CW, and CW/DW, (blue, red, and green, respectively).

contradicting the micromagnetic simulation of the equivalent state in Fig. 4b.

Finally, Fig. 5e shows the same initialised state again, except a CW vortex with domain wall (CW/DW) state was stabilised in the defect. Despite repeat attempts, it was not possible to isolate the eye-domain under the experimental LTEM conditions as the CW/DW state formed most readily. Under the applied field protocol, the same symmetric nanowire switching was observed in Fig. 5f as in Fig. 5d. The extra micrographs in Supplementary Fig. S9 in the SI show that the domain wall is initially pushed out of the defect, which resulted in the nanowire switch to the left of the defect and a stabilised CW vortex in the defect at $\mu_0 H_{||} = 7$ mT. Subsequently, the remaining CW vortex in the defect evolved in the same manner as the dataset represented in Fig. 5c, where the right nanowire switched at $\mu_0 H_{||} = 16$ mT.

To understand the experimental results of Fig. 5, the switching fields ($\mu_0 H_{sw}$) of the left and right nanowires (L and R, respectively) for the three conditions were compared in Fig. 5g, as well as the mode average switching field for the bulk lattice (see Methods). The initialised CCW vortex case showed a very large difference in the required in plane field magnitude required to switch the left and right nanowires ($\Delta\mu_0 H_{sw} = 19$ mT). The CCW vortex core migrated towards the top left of the figure under the increasing field before the defect saturated and induced the left nanowire switch, complimenting the results of the micromagnetic modelling in Fig. 4c(i-iii).

The left and right nanowires had highly similar switching fields in the initialised CW vortex condition, which contradicts the simulations. The right nanowire's switching field had reduced between the two chiralities ($\Delta\mu_0 H_{sw} = -10$ mT). Conversely, the switching field increased for the left nanowire ($\Delta\mu_0 H_{sw} = +6$ mT). It is evident that although an asymmetric effect is present within the system, it is not the dominating factor. The mechanism behind this is explored further in the discussion. By comparison, when the

defect was initialised with a CW/DW, the left nanowire switched at the same $\mu_0 H_{sw}$ magnitude as the CCW initialised state. In addition, the right nanowire switched at the same $\mu_0 H_{sw}$ as the CW state. This shows that the three initialised states achieved are distinguishable from each other under the experimental conditions. As the most populous initialised stabilised state, statistics were acquired on the vortex-DW states (Supplementary Fig. S10 in the SI) and showed good repeatability in the measurements.

Discussion

The HDASI system has been shown to promote the stabilisation of a plethora of metastable magnetic configurations within the hexagonal defect. Domain wall pinning locations are created from the combination of defect shape, as well as the magnetic coupling with the surrounding ASI lattice. The energetic degeneracy of the non-vortex magnetic states, as shown in the micromagnetic modelling in Fig. 2, promotes the formation of multiple metastable magnetic states in the hexagonal defect at remanence. It was shown in Supplementary Fig. S1 in the SI that a distribution of different states would form across the defect sites within a lattice. The ASI investigated is athermal due to the nominally large lattice thickness, which makes the nanowires insusceptible to thermal agitation. A study of the stochastic formation of states in thermal ASI defect systems could pose an interesting phase diagram subject to the thermal and magnetic field history, where the energetic degeneracy would have greater impact on the magnetic effects.

The in situ MFM study and subsequent probability distribution graph, in Fig. 3, shows distinct field windows for the favourable formations of the vortex, eye, and striped domain states, respectively. There is a preference for forming vortices at field magnitudes near $\mu_0 H = 20$ mT, when the field is applied along the armchair (*x*-) axis, whereas eye-domain formations are more prevalent at higher saturation fields ($\mu_0 H = 30$ mT). Striped domain states are dominant when the lattice is saturated in even higher applied fields in both the positive and negative field direction ($\mu_0 H = \pm 60$ mT), which restores the defect uniformity. The data shows that the magnetic state of the defects can be selected through the in plane field magnitude, but the impact of the localised magnetic switching in the ASI must also be considered. The localised field emanating from the defect is known to impact the switching field of the localised nanowires due to the increased magnetic flux density[19], but the surrounding magnetic state of the ASI mutually influences the stabilised structure of the defect's magnetic state when the applied field is released. The perturbing stray-field from the MFM probe when imaging the lattice, under an applied field, increases the efficacy of vortex formation once releasing the applied field. This is identified when comparing Fig. 3a(iv) to the micrographs used for the statistical analysis, where the lattice was not scanned with the MFM probe with the field applied. This effect is consistent with literature to return magnetic nanostructures to their ground state[38,39] and could be used to bias the defect state formation towards just vortices.

The results of Part A demonstrated that the HDASI lattice is a highly complicated system where the influence of the hexagonal defects on the ASI network, and vice versa, has to be considered. The simulated in plane angular dependence of nanowire switching, for an initial vortex state in the defect, demonstrates that there is a ~ 15° window, centred around 46°, where the HDASI magnetic switching mechanism is no longer symmetric. The simulations showed that the direction and sign of the injected emergent monopole was dependent on the chirality of the initial vortex in the defect and the applied field direction. Meanwhile, the evolution of the eye-domain's magnetic configuration under increasing field, at $\theta = 46°$, results in symmetric switching events in the two nanowires.

The asymmetric switching depends on a variety of factors including the defect geometry, topological protection of the vortex, and the localised magnetic coupling between the defect and surrounding nanowires. The high magnetic flux density localised at the vortex's core results in asymmetric switching as the core is displaced to the defect edge. In addition, the corner of hexagonal defects further concentrates the magnetic flux density at the defect-nanowire interface compared to a simple circular disk. This suggests logical selectivity for monopole injection based on the defect's magnetisation and the applied field angle, which is detectable by electrical methods such as magnetotransport and ferromagnetic resonance spectroscopy[40,41]. A defect-ASI system capable of both asymmetric and symmetric switching based on the initialised magnetic state of the defect could find applications in stochastic computing or reconfigurable waveguides.

The results of the modelling were tested through an experimental investigation in Fig. 5. The results of the simulations were well replicated for the case where the starting defect magnetisation was a CCW vortex. However, the results were less clear-cut when a CW vortex was initialised in the defect. There was a measurable change in nanowire switching fields on the left and right of the defect depending on the vortex chirality. However, for the initialised CW vortex, the similarity in switching fields for the left and right nanowires case was unexpected. The large difference of switching fields between the left and right nanowires for the CCW initialised state (Fig. 5g, blue), and the small magnitude difference in the CW initialised state (Fig. 5g, red), implies a type of field bias that was not replicated in the micromagnetic modelling.

A possible reason for this discrepancy between the experimental results and the simulations was that the OOP field present in the experiment has impacted the switching mechanism of the defect and surrounding nanowires. The simulations in Supplementary Fig. S5 of the SI showed that the OOP field reduced the in plane switching field of the defect more than the ASI nanowires due to its reduced shape anisotropy. This in turn disrupted the asymmetric nanowire switching fields in the simulations compared to the ideal case presented in Fig. 4. However, the modelling also suggested that the asymmetric switching would be diminished for both vortex chiralities and did not account for the asymmetric bias field effect recorded in Fig. 5. This demonstrates that the experimental HDASI system has more complex physics at play than the micromagnetic model can capture.

Despite the unknown source of the switching field bias, it is evident that the chirality of the defect does distinctly impact the localised switching field of the surrounding nanowires and could plausibly be used for selective injection with further optimisation of the experimental conditions and design of the lattice.

Conclusions

In conclusion, the investigation of an ASI system with hexagonal defects has revealed the significant role of defect lattice coupling on the stabilisation of metastable magnetic configurations and locally tuning the ASI switching response. The observed stabilisation and manipulation of metastable states in the hexagonal defects exhibit intriguing emergent phenomena, including stochasticity in the domain formation itself, as well as tailoring monopole injection characteristics in the ASI lattice. Furthermore, the manipulation of individual defects was shown to be effective in adapting the local switching fields of surrounding nanowires. Defects initialised with vortices of different chiralities were proposed as a mechanism for the asymmetric injection of monopoles, of opposite charge, within a low-field regime. Conversely, other initial magnetic configurations in the lattice did not produce the asymmetric switching behaviour. The experiments showed that the initial chirality of the defect magnetisation did affect the switching fields of the nanowires on the left and right of the defect. This provided evidence that the asymmetric switching mechanism was present in the system, albeit with an undetermined source of field bias. The findings provide valuable insights into the collective behaviour of nanomagnets in the ASI lattice and pave the way for future research in artificial frustrated materials and magnetic systems. Finely tuning the geometries of the system to include thermal effects could offer prospects in stochastic computing architectures, such as reservoir computing, or as reconfigurable waveguides based on the initial magnetic configurations of the defects in the lattice.

Methods

Film growth and ASI fabrication

The lattice is composed of elongated connected nanowires with an interior length of 800 nm and a width of 100 nm. This shape anisotropy forces their respective magnetisation to lie along their respective long axes. The hexagonal

defects are L = 1.60 μm (from point-to-point) and W = 1.39 μm (from edge-to-edge). For LTEM, the patterned Py structures were fabricated on Si_3N_4 membranes (t = 20 nm). Membranes were spin-coated with ZEP520A (t = 140 nm) and baked at 180 °C. The ASI arrays were then patterned by e-beam lithography (100 kV, 343 μC/cm^2) and developed in n-amyl acetate. Py (t = 20 nm, 2 Å/s) with a Pt capping layer to prevent oxidation (t = 2 nm, 1 Å/s) were evaporated. Finally, lift-off was performed in DMSO. For the MFM studies, ASI nanostructures were patterned using e-beam lithography with a combination of lift-off and Ar ion etching from a sputter-deposited film with a Si/SiO_x (300 nm)/Py (25 nm)/Pt (2 nm) film architecture.

Lorentz transmission electron microscopy

In LTEM, the electron beam deviates from the transmission path when it experiences a Lorentz force in the presence of a magnetic field. The direction of the electron beam's deflection is dependent on the magnetisation direction. In Fresnel mode, the image is defocused and the magnetically deflected electron beams of two neighbouring domains either overlap or deviate, resulting in bright or dark contrast, respectively. This change in contrast indicates the magnetisation direction normal to the beam path.

The LTEM measurements were conducted in Fresnel mode in a Hitachi HF-3300 (I2TEM) microscope operated at 300 kV and fitted with a cold field-emission gun and image corrector. The observations were done using the normal sample stage of the I2TEM with the objective lens switched off. Magnetic switching studies were performed by applying an in situ magnetic field and controlling the current of the objective lens of the microscope. As the magnetic field generated by the lens is oriented perpendicular to the image plane, the sample was tilted out of the imaging plane to apply external magnetic field components parallel to the sample plane. This results in both an out of plane (OOP) and in plane component of the applied field. The OOP field is considered constant throughout the data sequence as the small xz-tilt angles used result in a negligible variation in the OOP component in the interesting tilt range of the experiment. For example, a sample tilt of 2° is required to achieve an in plane field magnitude of 17.4 mT, which results in an OOP field component of 487.7 mT. This is only a 300 μT difference from zero-tilt. In Fig. 2, the planar saturation direction was modified by a few degrees to stabilise the different magnetic states. In Fig. 5, the sample was also rotated in its plane to adjust the direction of the applied field along different axes of the ASI network. The mode average for the switching field of the lattice was calculated by counting the frequency of switches at each field iteration for the three field sequence displayed. Subsequently the mean average of these three mode average switching fields is represented on the graph (dashed line).

The Transport of Intensity Equation (TIE) is a method employed for retrieving the phase shift introduced by the specimen on the electron beam. This phase shift is partly due to the magnetic properties of the studied system and can be used to map the in plane magnetic component integrated along the electron beam. The TIE is described within in-line holography technics and is based on the acquisition of images at different focal lengths (in general one under-focused, one over-focused and one in-focus). The images are then processed using an algorithm based on Fast Fourier Transform (FFT) before reconstructing the phase image. The gradient of the phase images, for a constant thickness and a homogeneous material, recovers the in plane (x and y) components of the magnetic induction[42].

Micromagnetic Modelling

OOMMF is a finite difference method solver for the Landau–Lifshitz–Gilbert (LLG) equation that calculates the total energy of regularly distributed discretised cells over the object domain. This is achieved by considering the summed influence of different micromagnetic energies on objects with predetermined magnetisation. The magnetisation within each cell is updated by a conjugate gradient energy evolver, which calculates the local energy minima directly. The energy-evolver is ideal for computationally larger structures, such as ASI lattices, as it allows the problem to reach convergence far quicker than the time-evolvers with the same result.

The component sizes of the modelled structures were conserved between simulations and experiments. The magnetic parameters of Py used for the micromagnetic modelling were taken from literature, where saturation magnetisation was assumed to be M_s = 860 kA/m and exchange constant J_{ex} = 13 pJ/m. The regularised mesh was comprised of 4 × 4 nm cells to best resolve the nanowire features. The image atlas was used to describe the structures with periodic boundary conditions extending in the y direction and with fixed boundary in x with width, w = 11.34 μm. The stopping criterion for the forward simulations was Max $|m\times H\times m| = 1e^{-6}$.

Magnetic Force Microscopy

MFM measurements were performed in traditional 2-pass tapping AFM mode, where the second pass is performed at a set distance away from the sample to record longer-range magnetostatic interactions between the magnetic probe and the sample in the absence of van der Waal topographical interactions. The measurements were performed in an NT MDT NTEGRA Aura microscope with an in-plane electromagnet mounted in situ, which was used to apply the field to the sample. All MFM measurements were performed at remanence unless otherwise stated. The angle of the field is applied along the image x-axis and approximately 1° from the lattice armchair axis direction. This field-lattice offset explains the greater population of eye-domains that form compared to Y-shaped domains, which is consistent with the micromagnetic modelling results presented in Fig. 2 and the surrounding text.

Data availability

The datasets generated and/or analysed during the current study are available from the corresponding author upon reasonable request.

Code availability

The code used in this study is available from the corresponding author upon reasonable request.

Received: 13 December 2023; Accepted: 14 August 2024;
Published online: 01 October 2024

References

1. Wang, R. F. et al. Artificial 'spin ice' in a geometrically frustrated lattice of nanoscale ferromagnetic islands. *Nature* **439**, 303–306 (2006).
2. Mengotti, E. et al. Real-space observation of emergent magnetic monopoles and associated Dirac strings in artificial kagome spin ice. *Nat. Phys.* **7**, 68–74 (2011).
3. Skjærvø, S. H., Marrows, C. H., Stamps, R. L. & Heyderman, L. J. Advances in artificial spin ice. *Nat. Rev. Phys.* **2**, 13–28 (2020).
4. Morgan, J. P., Stein, A., Langridge, S. & Marrows, C. H. Magnetic reversal of an artificial square ice: Dipolar correlation and charge ordering. *New J. Phys*. **13**, (2011).
5. Branford, W. R., Ladak, S., Read, D. E., Zeissler, K. & Cohen, L. F. Emerging Chirality in Artificial Spin Ice. *Sci. (80-.).* **335**, 1597–1600 (2012).
6. Kapaklis, V. et al. Thermal fluctuations in artificial spin ice. *Nat. Nanotechnol.* **9**, 514–519 (2014).
7. Saha, S. et al. Spin-Wave Dynamics and Symmetry Breaking in an Artificial Spin Ice. *Nano Lett.* **21**, 2382–2389 (2021).
8. Arava, H. et al. Control of emergent magnetic monopole currents in artificial spin ice. *Phys. Rev. B* **102**, 144413 (2020).
9. Arava, H. et al. Computational logic with square rings of nanomagnets. *Nanotechnology* **29**, (2018).
10. Arava, H. et al. Engineering Relaxation Pathways in Building Blocks of Artificial Spin Ice for Computation. *Phys. Rev. Appl.* **11**, 054086 (2019).
11. Gartside, J. C. et al. Reconfigurable training and reservoir computing in an artificial spin-vortex ice via spin-wave fingerprinting. *Nat. Nanotechnol.* **17**, 460–469 (2022).

12. Gilbert, I., Nisoli, C. & Schiffer, P. Frustration by design. *Phys. Today* **69**, 54–59 (2016).
13. Albisetti, E. et al. Nanopatterning spin-textures: A route to reconfigurable magnonics. *AIP Adv.* **7**, 055601 (2017).
14. Iacocca, E., Gliga, S. & Heinonen, O. G. Tailoring Spin-Wave Channels in a Reconfigurable Artificial Spin Ice. *Phys. Rev. Appl.* **13**, 1 (2020).
15. Gliga, S., Iacocca, E. & Heinonen, O. G. Dynamics of reconfigurable artificial spin ice: Toward magnonic functional materials. *APL Mater.* **8**, 040911 (2020).
16. Heyderman, L. J. *et al*. Mesoscopic magnetic systems: From fundamental properties to devices. *Appl. Phys. Lett*. **119**, (2021).
17. Gliga, S. et al. Emergent dynamic chirality in a thermally driven artificial spin ratchet. *Nat. Mater.* **16**, 1106–1112 (2017).
18. Östman, E. et al. Interaction modifiers in artificial spin ices. *Nat. Phys.* **14**, 375–379 (2018).
19. Puttock, R. et al. Defect-induced monopole injection and manipulation in artificial spin ice. *Nat. Commun.* **13**, 3641 (2022).
20. Drisko, J., Marsh, T. & Cumings, J. Topological frustration of artificial spin ice. *Nat. Commun.* **8**, 14009 (2017).
21. Sklenar, J. et al. Field-induced phase coexistence in an artificial spin ice. *Nat. Phys.* **15**, 191–195 (2019).
22. Lehmann, J., Donnelly, C., Derlet, P. M., Heyderman, L. J. & Fiebig, M. Poling of an artificial magneto-toroidal crystal. *Nat. Nanotechnol.* **14**, 141–144 (2019).
23. Puttock, R. et al. Modal Frustration and Periodicity Breaking in Artificial Spin Ice. *Small* **16**, 2003141 (2020).
24. Bhattacharjee, P. & Barman, S. Frequency Tunability of Spin-Torque Vortex Oscillator in Permalloy Nanodisks with Modified Material Properties. *Phys. status solidi – Rapid Res. Lett*. **17**, 2300056 (2023).
25. Shreya, S. et al. Granular vortex spin-torque nano oscillator for reservoir computing. *Sci. Rep.* **13**, 16722 (2023).
26. Shinjo, T., Okuno, T., Hassdorf, R., Shigeto, K. & Ono, T. Magnetic Vortex Core Observation in Circular Dots of Permalloy. *Sci. (80-.).* **289**, 930–932 (2000).
27. Fu, X. et al. Optical manipulation of magnetic vortices visualized in situ by Lorentz electron microscopy. *Sci. Adv.* **4**, 1–12 (2018).
28. Stenning, K. D. *et al*. Neuromorphic Few-Shot Learning: Generalization in Multilayer Physical Neural Networks. *arXiv* (2022).
29. Klaui, M., Vaz, C. A. F., Lopez-Diaz, L. & Bland, J. A. C. Vortex formation in narrow ferromagnetic rings. *J. Phys. Condens. Matter* **15**, R985–R1024 (2003).
30. Strandqvist, N. et al. Emergent anisotropy and textures in two dimensional magnetic arrays. *Phys. Rev. Mater.* **6**, 1–6 (2022).
31. Skovdal, B. E. et al. Temperature-induced collapse of spin dimensionality in magnetic metamaterials. *Phys. Rev. B* **104**, (2021).
32. Skovdal, B. E., Pálsson, G. K., Holdsworth, P. C. W. & Hjörvarsson, B. Emergent tricriticality in magnetic metamaterials. *Phys. Rev. B* **107**, 1–10 (2023).
33. Paganin, D. & Nugent, K. A. Noninterferometric Phase Imaging with Partially Coherent Light. *Phys. Rev. Lett.* **80**, 2586–2589 (1998).
34. Masseboeuf, A., Gatel, C., Marty, A., Toussaint, J. C. & Bayle-Guillemaud, P. Lorentz microscopy mapping during magnetization process of L10 FePd thin films. *J. Phys. Conf. Ser.* **126**, 0–4 (2008).
35. Rodríguez, L. A. et al. Quantitative in situ magnetization reversal studies in Lorentz microscopy and electron holography. *Ultramicroscopy* **134**, 144–154 (2013).
36. Porter, D. G. & Donahue, M. J. *OOMMF User's Guide, Version 1.0*. (1999).
37. Kazakova, O. et al. Frontiers of magnetic force microscopy. *J. Appl. Phys.* **125**, 060901 (2019).
38. Wang, Y.-L. et al. Rewritable artificial magnetic charge ice. *Sci. (80-.).* **352**, 962–966 (2016).
39. Gartside, J. C. et al. Realization of ground state in artificial kagome spin ice via topological defect-driven magnetic writing. *Nat. Nanotechnol.* **13**, 53–58 (2018).
40. Lendinez, S. & Jungfleisch, M. B. Magnetization dynamics in artificial spin ice. *J. Phys. Condens. Matter* **32**, 013001 (2020).
41. Kaffash, M. T., Lendinez, S. & Jungfleisch, M. B. Nanomagnonics with artificial spin ice. *Phys. Lett. A* **402**, 127364 (2021).
42. Zuo, C. et al. Transport of intensity equation: a tutorial. *Opt. Lasers Eng*. **135**, (2020).

Acknowledgements

This work was supported by the European Union's Horizon 2020 research and innovation programme under Grant agreement no. 823717—ESTEEM3. R.P. and O.K. acknowledge the support of the UK government department for Science, Innovation and Technology through NMS funding (Low Loss Electronics) and the UK national Quantum Technologies programme.

Author contributions

R.P. conceived the experiments, designed the artificial spin ice structures, performed the MFM measurements, analysed the experimental data, conducted the micromagnetic modelling, and wrote the manuscript. M.C.R conducted the ASI fabrication on SiN membranes for LTEM measurements, and A.F.S and H.W.S conducted the ASI fabrication on silicon for the MFM measurements. A.F., I.M.A., and C.G. conducted the LTEM measurements and TIE reconstruction. R.P., A.F., I.M.A, H.W.S, E.S., C.G. and O.K. were involved in discussions and critical assessment and analysis of the results. R.P. and O.K. coordinated the project. All authors contributed and reviewed the manuscript.

Competing interests

The authors declare no competing interests.

Additional information

Supplementary information The online version contains supplementary material available at https://doi.org/10.1038/s43246-024-00614-0.

Correspondence and requests for materials should be addressed to Robert Puttock or Olga Kazakova.

Peer review information *Communications materials* thanks Vassilios Kapaklis and the other, anonymous, reviewer(s) for their contribution to the peer review of this work. Primary Handling Editor: Aldo Isidori. A peer review file is available.